

Pressure-temperature phase diagram calculations using polynomial machine learning potentials: A comprehensive study based on global structure prediction and self-consistent phonon calculations

Hayato Wakai,^{1,*} Atsuto Seko,^{1,†} and Isao Tanaka¹

¹*Department of Materials Science and Engineering, Kyoto University, Kyoto 606-8501, Japan*

(Dated: March 31, 2025)

Polynomial machine learning potentials (MLPs) based on polynomial rotational invariants have been systematically developed for various systems and applied to efficiently predict crystal structures. In this study, we propose a robust methodology founded on polynomial MLPs to comprehensively enumerate crystal structures under high-pressure conditions and to evaluate their phase stability at finite temperatures. The proposed approach involves constructing polynomial MLPs with high predictive accuracy across a broad range of pressures, conducting reliable global structure searches, and performing exhaustive self-consistent phonon calculations. We demonstrate the effectiveness of this approach by examining elemental silicon at pressures up to 100 GPa and temperatures up to 1000 K, revealing stable phases across these conditions. The framework established in this study offers a powerful strategy for predicting crystal structures and phase stability under high-pressure and finite-temperature conditions.

I. INTRODUCTION

Many elemental systems and compounds are known to exhibit polymorphism, wherein they can crystallize into multiple distinct crystal structures. Notably, numerous polymorphs have been observed, especially under high-pressure conditions. For instance, experimental studies on elemental silicon (Si) have identified seven distinct phases that exist in sequence with increasing pressure: Si-I (diamond), Si-II (β -Sn), Si-XI (space group *Imma*), Si-V (simple hexagonal, SH), Si-VI (space group *Cmce*), Si-VII (hexagonal close-packed, HCP), and Si-X (face-centered cubic, FCC) within the pressure range of 0–100 GPa at room temperature [1–3]. To predict such crystal structures under varying pressure conditions, ranging from ambient to high pressures, global crystal structure searches using density functional theory (DFT) calculations have proven to be a powerful and effective tool [4–7].

Machine learning potentials (MLPs) have been widely used to perform large-scale simulations and a vast number of systematic calculations accurately and efficiently, which would be computationally expensive using DFT calculations [8–32]. These MLPs represent interatomic interactions by utilizing a range of structural features that describe the neighboring atomic distribution, in conjunction with machine learning models such as artificial neural networks, Gaussian process models, and linear models. Typically, MLPs are developed from extensive datasets derived from DFT calculations, which enables them to outperform conventional interatomic potentials in predicting various material properties. Recent studies have shown that MLPs significantly accelerate global structure searches by facilitating efficient energy and force calculations during local geometry optimizations

[33–39]. This acceleration allows for robust global structure searches across a wide search space, significantly reducing the likelihood of missing the true global minimum structures. The MLPs are also useful for performing reliable global structure searches under high-pressure conditions. Meanwhile, MLPs capable of accurately predicting a wide variety of structures under high-pressure conditions, including numerous hypothetical structures, are essential, and systematic global structure searches must be conducted.

Identifying globally stable structures at finite temperatures is also a computationally demanding task. To estimate phase stability at finite temperatures among local minimum structures obtained from global structure searches, self-consistent phonon approaches [40–44] can be employed with the effective use of MLPs. These approaches account for both harmonic and anharmonic vibrational effects and predict temperature-induced dynamical stability in structures that are dynamically unstable at lower temperatures. However, even when using MLPs, performing self-consistent phonon calculations in conjunction with global structure searches remains challenging for the following reasons. First, a comprehensive enumeration of structures with energy values close to the global minimum is necessary. Second, systematic free energy calculations using self-consistent phonon approaches must be performed for the enumerated local minimum structures. Such calculations are especially demanding for structures with fewer symmetry operations because they involve a large number of independent force-constant components, making the estimation of effective force constants computationally expensive. Furthermore, MLPs that can accurately perform self-consistent phonon calculations across various local minimum structures must be developed. Consequently, while MLPs are expected to be highly effective for identifying globally stable structures at finite temperatures, a comprehensive methodology combining global structure

* wakai@cms.mtl.kyoto-u.ac.jp

† seko@cms.mtl.kyoto-u.ac.jp

searches and free energy evaluations remains indispensable.

This study presents an efficient and robust approach that utilizes MLPs for crystal structure predictions under various pressure and temperature conditions. The performance of the proposed procedure is evaluated using elemental Si, which exhibits several experimentally observed polymorphs. To comprehensively and globally enumerate local minimum structures, this study employs an iterative procedure that combines random structure search (RSS) with the development of an MLP, which demonstrates high predictive power across a wide range of structures. This methodology has been previously applied in global structure searches using the polynomial MLP [37–39]. Subsequently, the stochastic self-consistent harmonic approximation (SSCHA) [45–47] is employed to investigate the phase stability among the local minimum structures identified through the global structure search. The polynomial MLP is used to perform the calculations required for this study. The polynomial MLP is constructed based on polynomial rotational invariants systematically derived from order parameters expressed in terms of radial and spherical harmonic functions. Polynomial MLPs developed for general purposes have demonstrated high predictive power across a wide range of crystalline [48–51] and liquid states [52].

An overview of the procedure proposed in this study is provided in Fig. 1, and the paper is organized as follows. Section II describes the formulation and construction procedure of the polynomial MLP. Section III presents a grid search approach for obtaining an optimal MLP, which is employed in the global structure search and phase stability analysis. Section III details the iterative procedure for a robust global structure search and presents the globally stable and metastable structures identified by the search. Section IV introduces the phase stability analysis procedure and provides the pressure-temperature phase diagram calculated using the proposed methodology. Section IV assesses both the computational requirements and the predictive accuracy of the MLP for SSCHA calculations. Finally, Sec. V concludes the study.

II. MLP DEVELOPMENT

A. Formulation of the polynomial MLP

In this section, the formulation of the polynomial MLP in elemental systems is presented [49, 53]. The short-range part of the potential energy for a structure, E , is assumed to be decomposed as $E = \sum_i E^{(i)}$, where $E^{(i)}$ denotes the contribution of interactions between atom i and its neighboring atoms within a given cutoff radius r_c , referred to as the atomic energy. The atomic energy is then approximately given by a function of invariants $\{d_m^{(i)}\}$ with any rotations centered at the position of atom

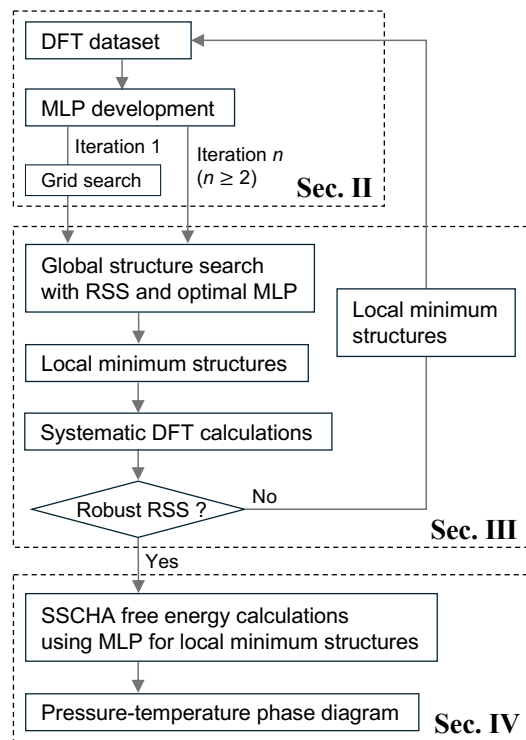


FIG. 1. Overview of the current procedure in this study. The dashed boxes and corresponding section numbers indicate the sections in which the respective topics are discussed.

i as

$$E^{(i)} = F\left(d_1^{(i)}, d_2^{(i)}, \dots\right), \quad (1)$$

where $d_m^{(i)}$ can be referred to as a structural feature for modeling the potential energy, and the polynomial MLP employs polynomial functions as function F .

When the neighboring atomic density is described by radial functions $\{f_n\}$ and spherical harmonics $\{Y_{lm}\}$, a p th-order polynomial invariant for radial index n and set of angular numbers $\{l_1, l_2, \dots, l_p\}$ is given by a linear combination of products of p order parameters, expressed as

$$d_{nl_1 l_2 \dots l_p, (\sigma)}^{(i)} = \sum_{m_1, m_2, \dots, m_p} c_{m_1 m_2 \dots m_p}^{l_1 l_2 \dots l_p, (\sigma)} a_{nl_1 m_1}^{(i)} a_{nl_2 m_2}^{(i)} \dots a_{nl_p m_p}^{(i)}, \quad (2)$$

where the order parameter $a_{nlm}^{(i)}$ is component nlm of the neighboring atomic density of atom i . The coefficient set $\{c_{m_1 m_2 \dots m_p}^{l_1 l_2 \dots l_p, (\sigma)}\}$ ensures that the linear combinations are invariant for arbitrary rotations, which can be enumerated using group-theoretical approaches such as the projection operator method [48, 54]. They are distinguished by index σ if necessary. The order parameter of atom i , $a_{nlm}^{(i)}$, is approximately evaluated from the neighboring atomic

distribution of atom i as

$$a_{nlm}^{(i)} = \sum_{\{j|r_{ij} \leq r_c\}} f_n(r_{ij}) Y_{lm}^*(\theta_{ij}, \phi_{ij}), \quad (3)$$

where $(r_{ij}, \theta_{ij}, \phi_{ij})$ denotes the spherical coordinates of neighboring atom j centered at the position of atom i . The current polynomial MLPs adopt a finite set of Gaussian-type radial functions modified by a cosine-based cutoff function to ensure smooth decay of the radial function [53].

Given a set of structural features $D^{(i)} = \{d_1^{(i)}, d_2^{(i)}, \dots\}$, the polynomial function F_ξ composed of all combinations of ξ structural features is represented as

$$\begin{aligned} F_1(D^{(i)}) &= \sum_s w_s d_s^{(i)} \\ F_2(D^{(i)}) &= \sum_{\{st\}} w_{st} d_s^{(i)} d_t^{(i)} \\ F_3(D^{(i)}) &= \sum_{\{stu\}} w_{stu} d_s^{(i)} d_t^{(i)} d_u^{(i)}, \end{aligned} \quad (4)$$

where w denotes a regression coefficient. A polynomial of the polynomial invariants $D^{(i)}$ is then described as

$$E^{(i)} = F_1(D^{(i)}) + F_2(D^{(i)}) + F_3(D^{(i)}) + \dots \quad (5)$$

In addition to the model given by Eq. (5), simpler models composed of a linear polynomial of structural features and a polynomial of a subset of the structural features are also introduced, such as

$$\begin{aligned} E^{(i)} &= F_1(D^{(i)}) + F_2(D_{\text{pair}}^{(i)} \cup D_2^{(i)}) \\ E^{(i)} &= F_1(D_{\text{pair}}^{(i)} \cup D_2^{(i)} \cup D_3^{(i)}), \end{aligned} \quad (6)$$

where subsets of $D^{(i)}$ are denoted by

$$D_{\text{pair}}^{(i)} = \{d_{n0}^{(i)}\}, D_2^{(i)} = \{d_{nll}^{(i)}\}, D_3^{(i)} = \{d_{nl_1l_2l_3}^{(i)}\}. \quad (7)$$

B. Hybrid polynomial MLP models

In this study, we propose an extended polynomial MLP model, which is represented as the sum of multiple polynomial MLP models using different sets of input parameters. Such a model will be referred to as a hybrid polynomial MLP model. The atomic energy in the hybrid polynomial MLP is expressed as the sum of two distinct MLP models, $E_{\text{mdl1}}^{(i)}$ and $E_{\text{mdl2}}^{(i)}$, given by

$$E^{(i)} = E_{\text{mdl1}}^{(i)} + E_{\text{mdl2}}^{(i)}, \quad (8)$$

where

$$\begin{aligned} E_{\text{mdl1}}^{(i)} &= F_1(D_{\text{mdl1}}^{(i)}) + F_2(D_{\text{mdl1}}^{(i)}) + \dots \\ E_{\text{mdl2}}^{(i)} &= F_1(D_{\text{mdl2}}^{(i)}) + F_2(D_{\text{mdl2}}^{(i)}) + \dots \end{aligned} \quad (9)$$

Here, $D_{\text{mdl1}}^{(i)}$ and $D_{\text{mdl2}}^{(i)}$ represent sets of structural features generated using different input parameter sets, such as the cutoff radius, the number of radial functions, and the truncation of polynomial invariants. Specifically, these parameters include the maximum angular momentum of spherical harmonics and the polynomial order of the invariants. These hybrid polynomial MLP models extend the framework presented in Eq. (5) and are expected to efficiently include a broader range of structural features derived from various input parameters, without requiring the consideration of intersection polynomials between the individual models.

The concept of hybrid models has been employed in several previous studies. For instance, attempts have been made to integrate MLPs with empirical interatomic potentials, such as the embedded atom method and bond-order potentials [55, 56]. Another example involves constructing interatomic potentials using two models with different cutoff radii, where one model captures short-range interactions and the other captures long-range interactions [57, 58]. The current hybrid polynomial MLP models follow a similar concept to the latter approach utilizing different cutoff radii.

C. Datasets

We begin the development of MLPs using a dataset from DFT calculations, comprising approximately 12,000 structures for elemental Si, which was previously developed in other studies [51, 53]. The procedure used to generate this dataset is summarized as follows. First, the atomic positions and lattice constants of 86 prototype structures [48] were optimized using DFT calculations under zero pressure. These prototypes consist of single elements with zero oxidation state from the Inorganic Crystal Structure Database (ICSD) [59], including metallic close-packed structures, covalent structures, layered structures, and those reported as high-pressure phases. Next, supercells of these optimized structures were used to introduce random lattice expansions, lattice distortions, and atomic displacements. DFT calculations were finally performed on these supercells to generate the dataset. This dataset will be referred to as dataset 1.

Dataset 1 is derived solely from prototype structures optimized at zero pressure and therefore includes only a limited number of structures with small volumes. As a result, the MLP trained on this dataset has relatively low predictive power for various properties under high-pressure conditions, as demonstrated later. To develop MLPs with higher predictive accuracy under high-pressure conditions, we generate additional structures from prototype structures optimized at elevated pressures using the following procedure.

First, the 86 prototype structures used to construct dataset 1 are optimized using DFT calculations at 25, 50, 75, and 100 GPa. Next, supercells of these optimized prototypes are used to create candidate structures

by randomly introducing lattice expansions, distortions, and atomic displacements, following the same procedure as dataset 1 [53]. A parameter controlling the upper bounds of the magnitude for these transformations is set to 0.3 Å. Finally, to reduce uncertainty more efficiently than random selection, we apply the structure-selection procedure described in Ref. [48], extracting a total of 4,000 structures from the candidate set. The dataset comprising these structures, combined with dataset 1, will be referred to as dataset 2. When the dataset is used to estimate MLPs through regression, it is randomly split into training and test sets, with 90 % allocated to training and 10 % to testing.

In this study, we performed DFT calculations for the additional 4,000 structures, following the computational conditions used for developing dataset 1. DFT calculations were carried out using the plane-wave-basis projector augmented wave (PAW) method [60, 61] within the Perdew–Burke–Ernzerhof (PBE) exchange–correlation functional [62] as implemented in the VASP code [63–65]. The cutoff energy was set to 400 eV, and the total energies were converged to less than 10^{-3} meV per supercell. The allowed spacing between k -points was approximately 0.09 \AA^{-1} . The configuration of the valence electrons in the PAW potential for Si is $3s^23p^2$.

Figure 2(a) shows the volume distributions for the structures in datasets 1 and 2. Dataset 2 combines all structures from dataset 1 with additional small-volume structures derived from prototype structures optimized under high pressures. Figure 2(b) shows the distributions of the coordination numbers around the atoms in the optimized prototype structures at 0, 25, 50, 75, and 100 GPa. We define the coordination number by counting neighbors within 1.2 times the nearest-neighbor atomic distance for each structure. These optimized prototypes exhibit diverse neighborhood environments and coordination numbers, which tend to increase as the optimization pressure rises.

D. MLP estimation

The regression coefficients of a potential energy model are estimated through linear regression using energy values, force components, and stress tensor components from the training dataset as observations. These quantities constitute the observation vector \mathbf{y} , while the corresponding structural features and their derivatives related to the force and stress tensors form the predictor matrix \mathbf{X} :

$$\mathbf{X} = \begin{bmatrix} \mathbf{X}_{\text{energy}} \\ \mathbf{X}_{\text{force}} \\ \mathbf{X}_{\text{stress}} \end{bmatrix}, \quad \mathbf{y} = \begin{bmatrix} \mathbf{y}_{\text{energy}} \\ \mathbf{y}_{\text{force}} \\ \mathbf{y}_{\text{stress}} \end{bmatrix}. \quad (10)$$

Here, $\mathbf{X}_{\text{energy}}$ contains polynomial features and their polynomial contributions to the total energy. The structural features for the force $\mathbf{X}_{\text{force}}$ and the stress tensor

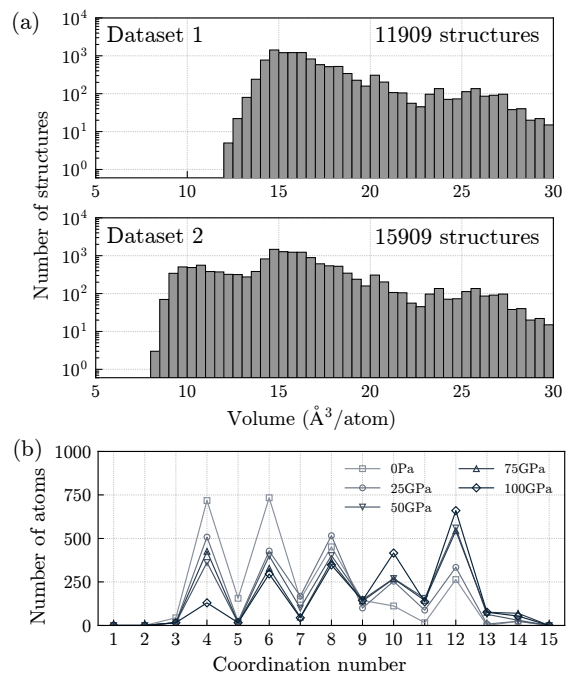


FIG. 2. (a) Volume distributions for the structures in datasets 1 and 2, displayed on a logarithmic scale for better visibility. (b) Distributions of the coordination numbers around atoms in the optimized prototype structures at 0, 25, 50, 75, and 100 GPa. The distributions for structures optimized under higher pressures are shown with darker lines.

$\mathbf{X}_{\text{stress}}$ are derived from derivatives of structural features, and their formulations were presented in Ref. [48]. The observation vector \mathbf{y} contains $\mathbf{y}_{\text{energy}}$, $\mathbf{y}_{\text{force}}$, and $\mathbf{y}_{\text{stress}}$, which consist of total energy entries, force entries, and stress tensor entries from the training dataset, respectively, computed using DFT calculations. The energy values and the stress tensor components are expressed in eV/cell, while the force components are expressed in eV/Å.

Weighted linear ridge regression is employed to estimate the regression coefficients \mathbf{w} . This regression method incorporates a penalty term to shrink the regression coefficients while minimizing the penalized residual sum of squares, expressed as

$$L(\mathbf{w}) = \|\mathbf{W}(\mathbf{X}\mathbf{w} - \mathbf{y})\|_2^2 + \lambda\|\mathbf{w}\|_2^2. \quad (11)$$

The solution for \mathbf{w} is obtained by solving the normal equations

$$(\mathbf{X}^T\mathbf{W}^2\mathbf{X} + \lambda\mathbf{I})\boldsymbol{\omega} = \mathbf{X}^T\mathbf{W}^2\mathbf{y}. \quad (12)$$

Here, λ represents the regularization parameter optimized to minimize prediction errors on the test set, and \mathbf{W} is a diagonal matrix whose entries weight the energy, force, and stress tensor data. The weight settings for the energy and force entries are consistent with those proposed in Ref. [38]. In these settings, larger weights are assigned to data entries with lower energy values and

smaller forces, which is critical for accurately modeling structures near local minima. To preserve high predictive accuracy of the regression model for the energy, force, and stress tensor data, the stress tensor entries are assigned relatively smaller weights than the energy entries.

E. MLP optimization

As demonstrated in Ref. [48], the accuracy and computational efficiency of the polynomial MLP are trade-off properties. We therefore obtain a set of Pareto-optimal MLPs with different trade-offs between these properties through a grid search. This search covers 523 single polynomial MLP models and 640 hybrid polynomial MLP models. In the single polynomial MLP models, the cutoff radius ranges from 4 to 12 Å, and polynomial invariants are considered up to approximately 25,000. In the hybrid polynomial MLP models, two separate models are combined. The first model uses smaller cutoff radii (4, 5, or 6 Å) and 3,000–25,000 polynomial invariants, capturing a wide range of coordination environments. The second model adopts larger cutoff radii (6, 7, 8, 10, or 12 Å) and a varying number of polynomial invariants (1,000 to 25,000). These polynomial MLPs are developed from datasets using the PYPOLYMLP code [53, 66].

Figure 3 shows the prediction error and computational efficiency of the polynomial MLPs obtained through the grid search for elemental Si. The prediction errors are evaluated using the root mean square errors (RMSEs) of the energy. To ensure practical relevance, these RMSEs are calculated using the test datasets that exclude structures with exceptionally high energies or large forces. The computational efficiency is assessed by measuring the elapsed time to compute the energy, forces, and stress tensors 10 times for a structure containing 1000 atoms. As the model complexity of the polynomial MLP increases, the prediction error generally decreases. Among the Pareto-optimal MLPs, the polynomial MLPs constructed using hybrid polynomial MLP models demonstrate lower prediction errors than those constructed with single polynomial MLP models when the computational cost exceeds 1.5 ms/step/atom. Hence, the hybrid polynomial MLPs can provide Pareto-optimal MLPs with a better trade-off between prediction error and computational cost.

A reasonable MLP with a computational time of 3.1 ms/atom/step is selected from the set of Pareto-optimal MLPs, balancing prediction accuracy and efficiency. It is designated as the optimal MLP for performing global structure searches and phase stability analyses, as indicated by the red closed square in Fig. 3. Its RMSEs for energy, force, and stress tensor are 2.8 meV/atom, 0.055 eV/Å, and 35.9 meV/atom, respectively. Figure 4(a) compares cohesive energies for all optimized prototype structures at pressures ranging from 0 to 100 GPa calculated by both the DFT and the optimal MLP. In most cases, the MLP yields minor errors across differ-

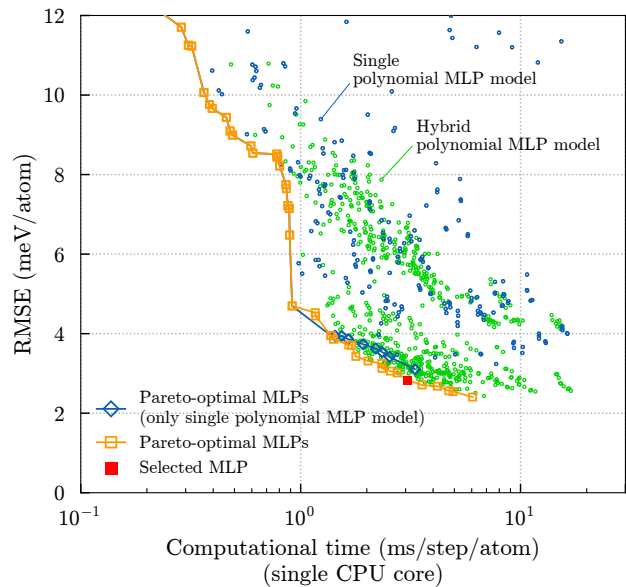


FIG. 3. Prediction error and computational efficiency of polynomial MLPs obtained from the grid search in elemental Si. The blue and green open circles represent the properties of MLPs constructed using single polynomial MLP models and hybrid polynomial MLP models, respectively. Computational efficiency is assessed based on the computation time using a single core of the Intel[®] Xeon[®] E5-2630 v3 (2.40 GHz). The orange open squares denote the Pareto-optimal MLPs across both single and hybrid polynomial MLP models, while the blue open diamonds represent the Pareto-optimal MLPs from the single polynomial MLP models only. The red closed square indicates the selected MLP for conducting the global structure search and phase stability analysis.

ent pressure conditions. Figure 4 also presents the distributions of (b) cohesive energy values, (c) force components, and (d) stress tensor components for dataset 2. The MLP produces narrow error distributions in all three categories, demonstrating high predictive accuracy for diverse structures and local environments, as illustrated in Fig. 2(b).

F. Predictive power

Here, we present the predictive capability of the optimal MLP for the energy-volume curve and phonon properties. Datasets 1 and 2, shown in Fig. 2, are used to train two different MLPs, which are then applied to calculate the energy-volume curve and phonon properties. The key difference between these datasets is that dataset 2 includes random structures derived from prototype structures optimized under high pressure. This section demonstrates that achieving high predictive accuracy under elevated pressures requires incorporating random structures derived from high-pressure optimized prototypes.

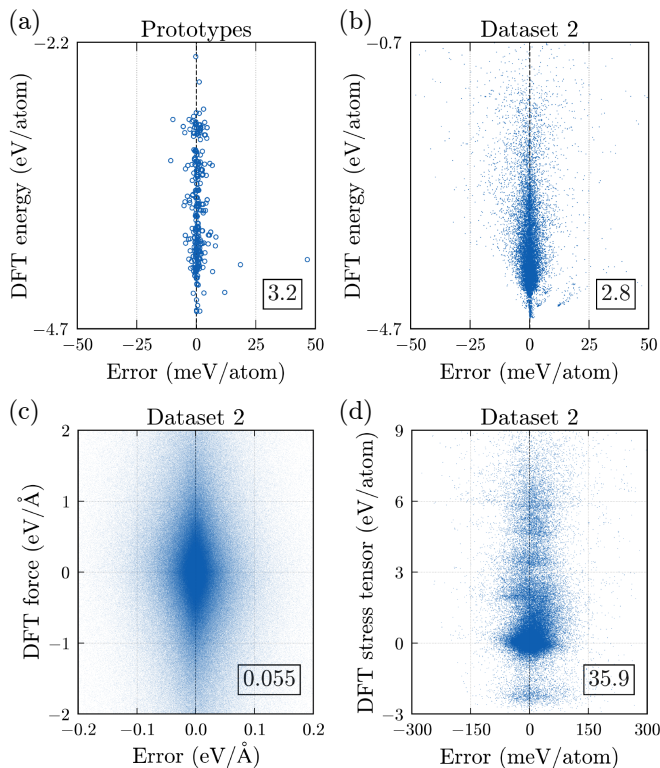


FIG. 4. (a) Distribution of the cohesive energy for all prototype structures optimized at pressures ranging from 0 to 100 GPa. Distributions of (b) cohesive energy values, (c) forces, and (d) stress tensor components for dataset 2 are presented. They are calculated using the optimal MLP. The numerical values enclosed in squares represent the RMSEs for energy, force, and stress tensor components, expressed in units of meV/atom, eV/Å, and meV/atom, respectively. In panels (b), (c), and (d), the RMSEs are computed using the test dataset.

1. Energy-volume curves

Figure 5 shows the energy-volume curves of the diamond-, β -Sn-, SH-, Si-VI-, HCP-, and FCC-type structures in elemental Si. These structures have been experimentally observed at 0–100 GPa and room temperature. We compare energy-volume curves computed using the DFT with those from two MLPs. In the small-volume region, the MLP constructed from dataset 1 deviates from the DFT values due to the insufficient number of small-volume structures in dataset 1. In contrast, the MLP developed using dataset 2 accurately reproduces the DFT results for all structures.

2. Phonon properties

Figure 6 presents the phonon density of states (DOS) for diamond-, β -Sn-, SH-, Si-VI-, HCP-, and FCC-type structures at 50 GPa in elemental Si. These calculations are performed using the DFT and the two MLPs within

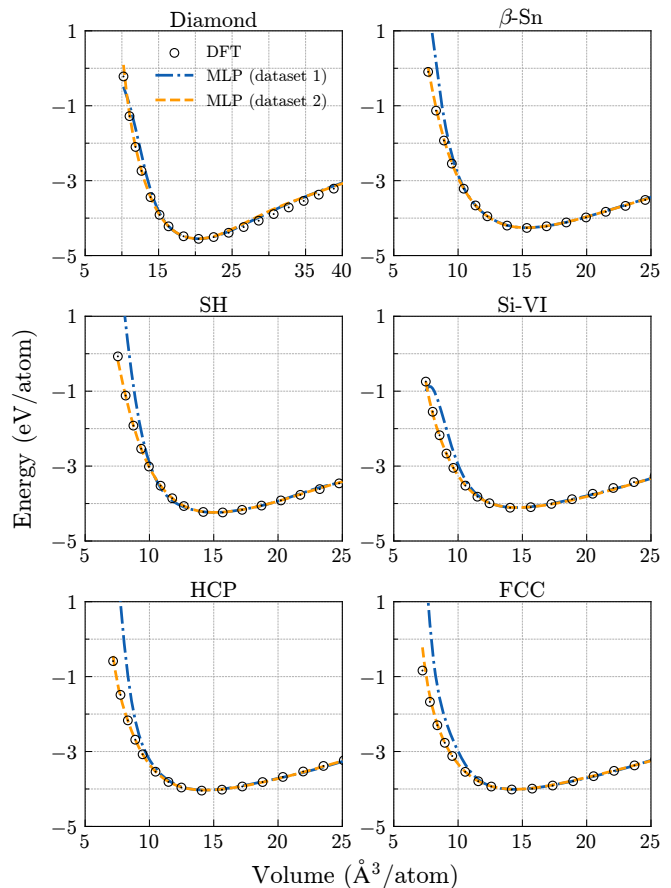


FIG. 5. Energy-volume curves of the diamond-, β -Sn-, SH-, Si-VI-, HCP-, and FCC-type structures, computed using the DFT calculation and MLPs developed from datasets 1 and 2 for elemental Si. Dataset 2 includes random structures derived from prototype structures optimized at high pressures.

the harmonic approximation. The finite displacement method in PHONOPY code [67] is employed to obtain phonon properties and thermal expansion, with supercells constructed by expanding the conventional unit cells of the respective structures. The phonon DOS calculated with the MLP constructed from dataset 1 is inconsistent with the DFT results, especially for the FCC-type structure. By comparison, the phonon DOS obtained using the MLP from dataset 2 agrees with the DFT results.

Figure 7 shows the temperature dependence of thermal expansion, calculated using the quasi-harmonic approximation, for the β -Sn-, SH-, HCP-, and FCC-type structures at 10, 30, 50, and 90 GPa, respectively. Although developing MLPs that accurately predict thermal expansion is more challenging than those designed to predict phonon DOS, the MLP developed from dataset 2 accurately predicts thermal expansion. By contrast, the MLP trained on dataset 1 produces inconsistent results and cannot compute the thermal expansion for the FCC-type structure because it predicts the FCC-type structure to be dynamically unstable.

Note that dataset 2 consists of approximately 16,000

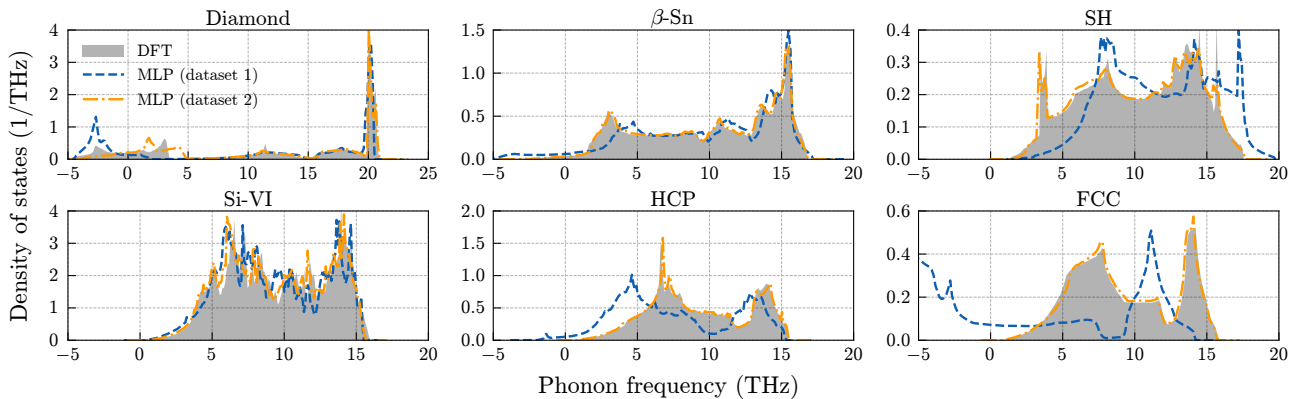


FIG. 6. Phonon DOS for diamond-, β -Sn-, SH-, Si-VI-, HCP-, and FCC-type structures at 50 GPa in elemental Si. These are computed using DFT calculations and MLPs developed using datasets 1 and 2 within the harmonic approximation. The shaded region represents the phonon DOS obtained using the DFT calculation.

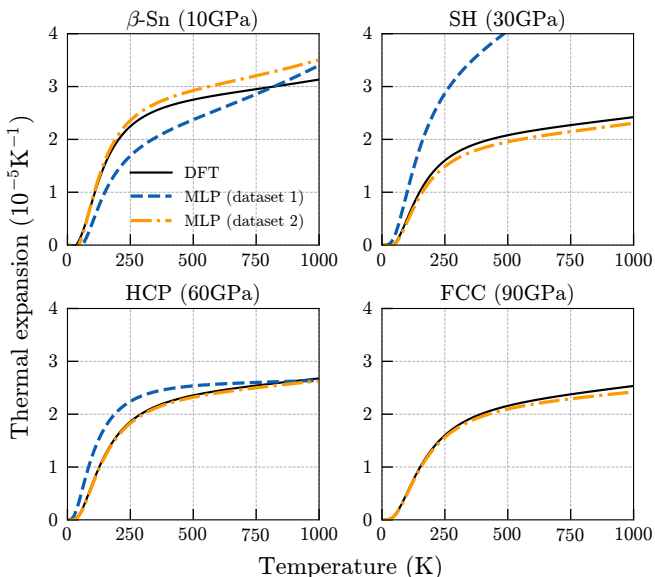


FIG. 7. Temperature dependence of the thermal expansion in β -Sn-, SH-, HCP-, and FCC-type structures at 10, 30, 60, and 90 GPa, respectively, for elemental Si. These are computed using DFT calculations and MLPs developed using datasets 1 and 2 within the quasi-harmonic approximation.

structures, of which 4,000 are random structures derived from prototype structures optimized at high pressures. Even though these random structures account for only about one-fourth of the dataset, they significantly enhance the predictive power of the polynomial MLP for the energy-volume curve and phonon properties under high-pressure conditions. Furthermore, this improvement does not depend on any specific MLP choice, since other Pareto-optimal MLPs also show consistently high accuracy. Therefore, the current dataset provides sufficient information to enable accurate predictions under high-pressure conditions.

III. STRUCTURE ENUMERATION

A. Methodology and search space

We employ an RSS method to enumerate globally stable and metastable structures, which corresponds to the multi-start method in global optimization [68]. In this approach, local geometry optimizations are repeatedly performed on random initial structures, and the local minimum structure with the lowest enthalpy is considered the global minimum. This heuristic approach has been previously utilized in the *ab initio* random structure search (AIRSS) [4, 33].

In this study, to perform the RSS at various pressures for elemental Si, we generate initial structures by randomly assigning lattice parameters and fractional atomic coordinates in the primitive cells. The maximum number of atoms defining the degrees of freedom for structure optimization is restricted to 16. We set the maximum volume per atom for an initial structure to ten times the atomic sphere volume, which is determined from the nearest-neighbor distance of the equilibrium diamond-type structure obtained from the DFT calculation. We also discard structures that contain atomic pairs separated by excessively short distances. This step is unavoidable because geometry optimizations starting from such structures with the current polynomial MLP often fail or converge to anomalous structures exhibiting significantly negative energy values. These constraints only prevent the generation of structures with excessively large volumes or extremely short interatomic distances, thereby enabling a systematic global structure search across a wide search space without relying on prior knowledge.

B. Iterative update of MLP

We utilize the optimal MLP described in Sec. II E for the global structure search. This MLP is selected from

among Pareto-optimal MLPs to balance prediction accuracy for energy and computational efficiency. Although the MLP exhibits high predictive power for various structures, it occasionally predicts incorrect local minimum structures and fails to accurately estimate their energy values.

To enhance the robustness of the global structure search, the MLP is iteratively updated through repeated global structure searches, as follows. Single-point DFT calculations are performed on all local minimum structures identified by the RSS with the MLP, and these results are added to the training dataset. We then retrain the MLP with this expanded dataset and repeat the global structure search using the updated MLP. This iterative approach, which combines the polynomial MLP and RSS, has been previously employed in global structure searches utilizing the polynomial MLP [37–39].

C. Computational details

The current global structure search using the MLP is performed in three iterations. In the first iteration, we limit the unit cell to a maximum of 8 atoms, while in the second and third iterations, we allow up to 16 atoms. Local geometry optimizations are carried out at pressures up to 100 GPa, with a grid spacing of 5 GPa, covering a total of 21 pressure conditions. For each pressure, we generate 1,000 initial structures for systems with up to 8 atoms and 500 initial structures for those with 9–16 atoms. In total, 168,000 structures are randomly generated in the first iteration, and 252,000 structures are randomly generated in the second and third iterations. In the second and third iterations, local geometry optimizations are performed not only for newly generated random structures but also for the local minimum structures identified in previous iterations. This approach enables the efficient and comprehensive enumeration of local minimum structures.

D. Accuracy of updated MLP

Figure 8 shows the distributions of $E + \bar{\sigma}V$ for local minimum structures obtained in both the first and final iterations, evaluated by the MLPs and DFT calculations. The distribution for each iteration is obtained using the MLP applied at the corresponding iteration. Here, E represents the cohesive energy, V denotes the cell volume, and $\bar{\sigma}$ is the mean normal stress, defined as $\bar{\sigma} = (\sigma_{11} + \sigma_{22} + \sigma_{33})/3$ [69], where σ_{ij} denotes the stress component acting in the j direction on a plane normal to the i direction. In the first iteration, many local minimum structures exhibit large prediction errors. However, by incorporating these structures and their DFT-computed properties into the training dataset and retraining the MLP, the predictive accuracy for local min-

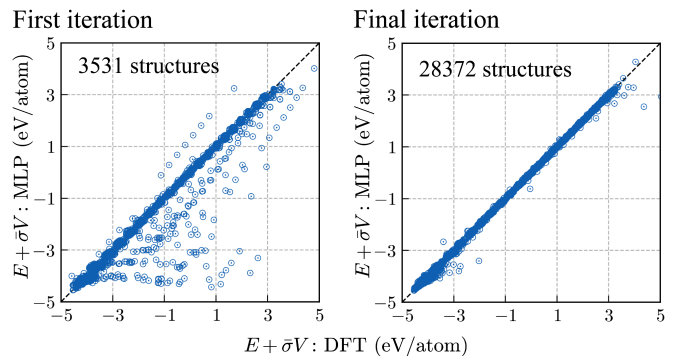


FIG. 8. Distributions of $E + \bar{\sigma}V$ for local minimum structures, computed using both the MLPs and DFT calculations, at the first and final iterations of the iterative MLP update procedure.

imum structures improves significantly in the final iteration.

Note that the enthalpy of a local minimum structure is given by $E + pV$ when the stress tensor satisfies $\sigma_{ij} = p\delta_{ij}$, where δ_{ij} is the Kronecker delta. In Fig. 8, the stress tensor of the local minimum structure optimized by the MLP is evaluated through a single-point DFT calculation. Because of prediction errors in the MLP, DFT stress tensor components deviate from the condition $\sigma_{ij} = p\delta_{ij}$. Consequently, the DFT enthalpy value of the local minimum structure cannot be directly obtained from a single-point DFT calculation. Therefore, Fig. 8 instead presents the distributions of the alternative measure $E + \bar{\sigma}V$, which serves as an approximate evaluation of the predictive accuracy for enthalpy.

E. Globally stable and metastable structures

By performing the RSS with the updated MLP for elemental Si, we enumerate a total of 28,372 local minimum structures. Figure 9(a) presents their relative enthalpy values computed by the MLP. At each pressure, the relative enthalpy is defined with respect to the lowest enthalpy value among the local minimum structures found at the corresponding pressure. The MLP enables the enumeration of numerous structures across all pressure settings. However, the enthalpy values predicted by the MLP still exhibit small but non-negligible prediction errors. Therefore, we compute their enthalpy values using DFT calculations to evaluate the phase stability among these local minimum structures, as follows. First, we select 344 local minimum structures with MLP-calculated relative enthalpies below 30 meV/atom, as shown in Fig. 9(a). We then perform DFT-based geometry optimizations for these structures and eliminate duplicates.

Geometry optimizations were performed using DFT calculations under more demanding computational conditions compared to those applied in the MLP development. The cutoff energy was set to 600 eV, and the al-

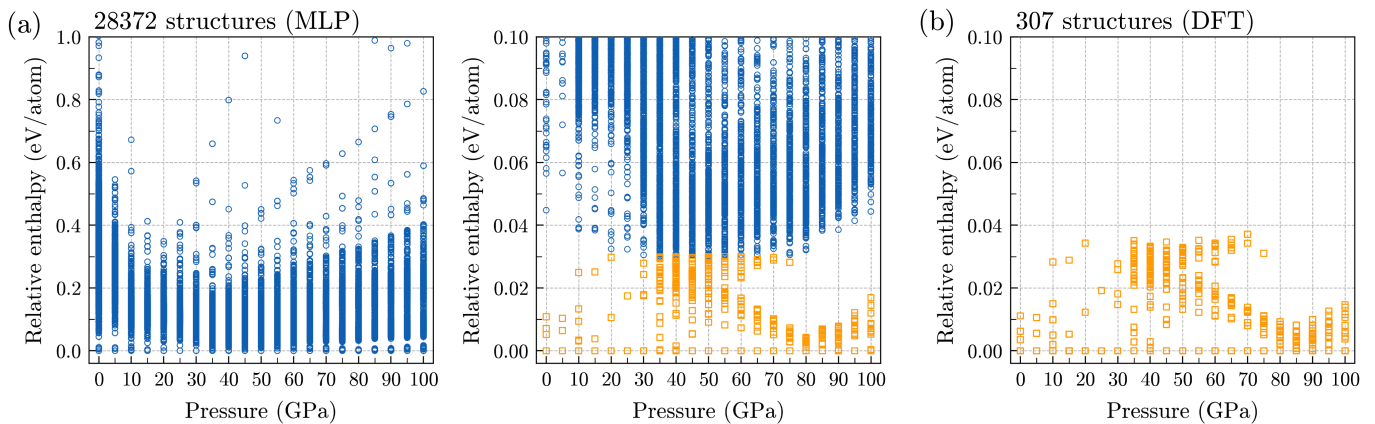


FIG. 9. (a) Relative enthalpy values of local minimum structures computed using the MLP for elemental Si. In the left and central panels, the maximum values of the vertical axis are set to 1.0 and 0.1 eV/atom, respectively. The orange open squares represent structures with relative enthalpy values below 30 meV/atom, as computed by the MLP. (b) Relative enthalpy values of the structures indicated by the orange open squares in (a), obtained through geometry optimizations using DFT calculations.

TABLE I. Global minimum structures identified through the current global structure search for elemental Si. The pressure ranges where these structures are global minima, as estimated from DFT calculations, are shown. The experimentally reported pressure ranges at room temperature are also provided [1–3]. The pressure ranges are expressed in GPa. Z denotes the number of atoms in the unit cell. Although the Si-XI structure is not found in the global structure search, the pressure range where the Si-XI structure is the global minimum is evaluated and indicated in parentheses.

Space group	Z	ICSD-ID	Prototype	Calc.	Exp.
$Fd\bar{3}m$	8	51688	Si-I (diamond)	0–9.8	0–11
$I4_1/amd$	4	52460	Si-II (β -Sn)	9.8–11.3	11–13
$Imma$	4	41392	Si-XI	(10.6–11.4)	13–16
$P6/mmm$	1	52456	Si-V (SH)	11.3–33.5	16–38
$Cmce$	16	89414	Si-VI	33.5–39.6	38–42
$P6_3/mmc$	2	52459	Si-VII (HCP)	39.6–83.8	42–79
$P6_3/mmc$	4	—	α -La	83.8–87.7	—
$Fm\bar{3}m$	4	52458	Si-X (FCC)	87.7–	79–

lowed spacing between k -points was approximately set to 0.07 \AA^{-1} . For the local minimum structures with relative enthalpy values below 10 meV/atom at specific pressure conditions, we further relaxed them using a finer k -point grid spacing of 0.05 \AA^{-1} . The atomic positions and lattice constants were optimized until the residual forces were less than 10^{-4} eV/\AA .

Figure 9(b) presents the DFT-calculated relative enthalpy values of 307 local minimum structures. As shown in Figs. 9(a) and (b), the MLP-calculated relative enthalpy distribution closely agrees with that computed using the DFT. This consistency demonstrates that combining the MLP with the RSS accurately enumerates local minimum structures with low relative enthalpy values.

To evaluate the stability of the local minimum struc-

tures across the entire pressure range of 0–100 GPa, we compute energy values at various volumes for these structures using DFT calculations. We then fit these volume-energy datasets to the Rose–Vinet equation of state (EOS) [70], allowing us to estimate the enthalpy of each structure across the entire pressure range. Table I lists the global minimum structures found within 0–100 GPa and the corresponding pressure ranges where these structures are globally stable. The experimentally reported pressure ranges at room temperature are also provided [1–3]. Among the structures reported experimentally, Si-I (diamond) [71], Si-II (β -Sn) [72], Si-V (SH) [73], Si-VI [2], Si-VII (HCP) [73], and Si-X (FCC) [74] structures are calculated to be global minima, and their predicted pressure ranges closely match the experimental ones. The α -La-type structure is identified as the global minimum structure, although no experimental data for this phase has been reported.

Although the Si-XI structure has been reported experimentally [75], it was not identified in the global structure search. To validate this result, we performed geometry optimizations starting from the experimental Si-XI structure over a fine pressure grid from 8 to 15 GPa. Using DFT calculations with a convergence criterion of 10^{-4} eV/\AA , we found that Si-XI remains a local minimum between 9.8 and 11.6 GPa, whereas at other pressures it transforms into β -Sn- or SH-type structures. In contrast, under the same convergence criterion, MLP-based geometry optimizations resulted in relaxation into β -Sn- or SH-type structures over the entire 8–15 GPa range. This result is consistent with the absence of the Si-XI structure in the MLP-based structural search. However, when a less strict convergence criterion of 10^{-2} eV/\AA was applied in the MLP-based optimization, the Si-XI structure remained a local minimum structure within the 11.8 to 13.1 GPa range. This observation indicates that the enthalpy values for the Si-XI, β -Sn-type, and SH-type structures are closely comparable, suggesting that the potential en-

TABLE II. Metastable local minimum structures, which are the same as experimentally reported structures [76–79]. The relative enthalpy value ΔH calculated at specific pressures (in GPa) is expressed in meV/atom. If the relative enthalpy value predicted by the MLP is less than 30 meV/atom, the relative enthalpy value calculated using DFT is provided. Otherwise, the value predicted by the MLP is given in parentheses.

Space group	Z	ICSD-ID	Prototype	ΔH	Pressure
$Cmcm$	24	25241	—	(110.4)	0
$P6_3/mmc$	4	30101	Si-IV	11.6	5
$Ia\bar{3}$	16	246372	Si-III	(38.8)	10
$R\bar{3}$	24	109036	Si-XII	(39.1)	10

ergy surface around the Si-XI structure is near that of a saddle point. Accurately capturing this behavior with the MLP remains a significant challenge.

To evaluate the phase stability of the Si-XI structure, we obtain the enthalpy values of DFT-optimized structures in the 9.8–11.6 GPa range from the preceding validation. Subsequently, isotropic compression is applied to the converged structure, and the corresponding energy values are computed using DFT calculations. By fitting the volume-energy data, the EOS curve for the Si-XI structure is derived. As a result, the Si-XI structure is found to be globally stable within the 10.6–11.4 GPa range.

Table II lists the metastable local minimum structures, which correspond to experimentally reported structures [76–79]. Although the Si-XI structure is not identified in the current global structure search, as mentioned above, all other experimentally reported structures are discovered. We evaluate their enthalpy values using DFT calculations if the MLP predicts enthalpies below 30 meV/atom; otherwise, we use the MLP-calculated values. These structures exhibit positive relative enthalpy values, which is consistent with the fact that they have not been observed as stable structures in experiments. The Si-III structure has been reported as a metastable phase, obtained through slow pressure release from the high-pressure β -Sn phase [76]. The Si-XII structure was also experimentally obtained by pressure release from the β -Sn phase and exists over a relatively wide pressure range of 2–12 GPa [77]. The structure with space group $Cmcm$ was synthesized using a high-pressure precursor method and $\text{Na}_4\text{Si}_{24}$ precursor [78]. The Si-IV structure [79] was synthesized by heating the Si-III structure at 200–600 °C [80].

Figure 10 presents the relative enthalpy values for local minimum structures computed by DFT calculations. Structures with relative enthalpy values exceeding 10 meV/atom over the entire pressure range are excluded from Fig. 10. In addition to the stable structures listed in Table I, three metastable local minimum structures are identified in the 0–80 GPa range in Fig. 10(a). They correspond to the Si-IV structure, a structure with space group $I4_1/acd$ represented with 32 atoms, and a struc-

ture with space group $R\bar{3}m$. Moreover, it is also observed that the enthalpy values of the Si-XI structure are nearly identical to those of the β -Sn-type structures. Between 80 and 100 GPa in Fig. 10(b), 15 metastable structures with low relative enthalpy values are found. These structures exhibit different stacking orders of close-packed planes, indicating that elemental Si tends to adopt close-packed structures under high pressures.

IV. PHASE STABILITY AT FINITE TEMPERATURE

In this section, we investigate the phase stability at finite temperatures for the local minimum structures identified through the global structure search in elemental Si. To evaluate their free energies, we employ the SSCHA method. The SSCHA method provides a more accurate evaluation of free energy at high temperatures compared to the harmonic approximation. Moreover, this method can predict the dynamical stability of structures that are dynamically unstable under the harmonic approximation.

A. SSCHA formulation

Firstly, we outline the formulation of the SSCHA for a given volume and temperature. In the SSCHA [45–47], the free energy is expressed by

$$F_{\text{SSCHA}} = F_{\theta} + \frac{1}{N_{\text{samp}}} \sum_{s=1}^{N_{\text{samp}}} \left[V_{\text{BO}}^{(s)} - \mathcal{V}^{(s)} \right], \quad (13)$$

where F_{θ} represents the harmonic expression of the free energy, which is calculated using the effective harmonic force constants (FCs) θ . $V_{\text{BO}}^{(s)}$ and $\mathcal{V}^{(s)}$ correspond to the Born–Oppenheimer energy and the harmonic potential of the s -th sample structure, respectively. The differences between these quantities are averaged over N_{samp} sample structures, which are generated from the density matrix at temperature T with FCs θ . A detailed formulation of Eq. (13) and the density matrix can be found in Ref. [45]. The SSCHA effectively captures the temperature dependence of phonon frequencies and incorporates anharmonic contributions into the free energy calculation.

We employ an iterative procedure to optimize the effective harmonic FCs [81]. Initially, the effective harmonic FCs are provided using a selected strategy. Subsequently, a displacement-force dataset consisting of N_{samp} sample structures is generated using the polynomial MLP. The updated FCs are then estimated from this dataset using standard linear regression. This estimation process is implemented in the SYMFC code [82], which facilitates efficient FC estimation even for structures with many independent FC components. The procedure of generating sample structures and updating the FCs is iteratively repeated until the FCs converge. Finally, the SSCHA free

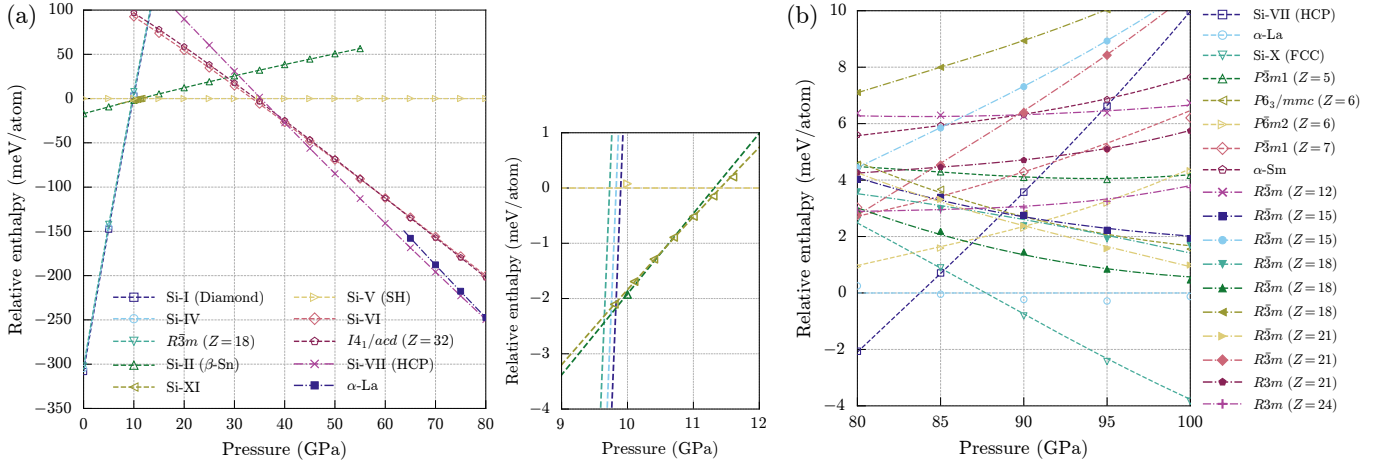


FIG. 10. Relative enthalpy values computed using DFT calculations for local minimum structures. Local minimum structures with relative enthalpy values exceeding 10 meV/atom across the entire pressure range are excluded from the analysis. The legend indicates the space groups of the structures or their corresponding prototype structures, and Z denotes the number of atoms in the unit cell. (a) Enthalpy values are shown relative to the Si-V structure for pressures from 0 to 80 GPa in the left panel. The relative enthalpies in the central panel are displayed for the 9–12 GPa range, where multiple structures have very similar enthalpy values. (b) Enthalpy values are shown relative to the α -La-type structure for pressures from 80 to 100 GPa.

energy is obtained from Eq. (13) using the energy and force values of the sample structures computed with the MLP.

The iterative process is terminated when the relative change in the FCs becomes smaller than a specified threshold, ε_{FC} , as defined by

$$\frac{\|\boldsymbol{\theta}_{[l]} - \boldsymbol{\theta}_{[l-1]}\|_2}{\|\boldsymbol{\theta}_{[l-1]}\|_2} < \varepsilon_{\text{FC}}, \quad (14)$$

where $\boldsymbol{\theta}_{[l]}$ represents the FCs at iteration step l , and $\|\cdot\|_2$ denotes the L_2 norm. In this study, the threshold ε_{FC} is set to 0.01. To stabilize the convergence of the SSCHA iterations, a mixing scheme is applied when updating the FCs. The updated FCs are given by

$$\boldsymbol{\theta}_{\text{mix}[l]} = \alpha \boldsymbol{\theta}_{[l]} + (1 - \alpha) \boldsymbol{\theta}_{[l-1]}, \quad (15)$$

where the mixing parameter α is set to 0.5 in this study. The current procedure for SSCHA calculations, coupled with polynomial MLPs, is implemented in the PYPOLYMLP code [53, 66]. Calculations based on the FCs, similar to those used in the harmonic approximation, are performed using the PHONOPY code [67].

B. Computational procedures

In this study, a slightly complicated procedure is introduced to accurately evaluate phase stability while reducing computational cost. A workflow of the current procedure to evaluate the phase stability of local minimum structures is shown in Fig. 11. Firstly, 80 structures are selected from the local minima identified through the global structure search. These structures are those with

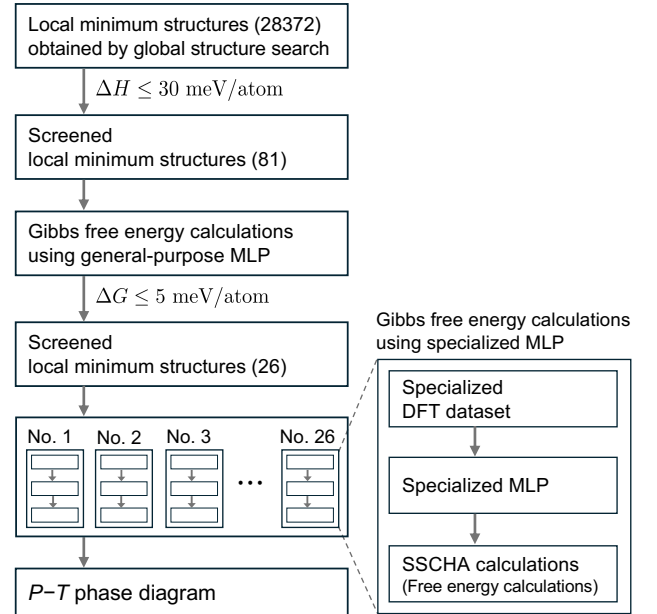


FIG. 11. Workflow of the current procedure for calculating the phase diagram from the global structure search. The numbers in parentheses represent the number of structures obtained in this study. ΔH and ΔG denote the relative enthalpy and relative Gibbs free energy, respectively.

relative enthalpy values below 30 meV/atom, as represented by the orange open squares in Fig. 9(a). Note that the total number of orange open squares in Fig. 9(a) exceeds 80 because some structures at different pressures correspond to the same structural types, such as FCC and HCP. After eliminating these duplicates, 80 unique structures are obtained. The phase stability analysis is

performed on 81 local minimum structures, including the 80 unique structures in addition to the Si-XI structure.

Subsequently, the volume dependence of the Helmholtz free energy is computed for the selected structures using the SSCHA over a range of temperatures. For each structure, 10 to 20 distinct volumes are considered, and equilibrium configurations at these volumes are determined using the MLP. In cases where the structure transforms into a different type during MLP-based geometry optimization, the configuration for a given volume is obtained by isotropically adjusting the volume of the structure at a reference volume where it remains stable. SSCHA calculations are conducted using supercells containing between 64 and 216 atoms, and the number of sample structures in each SSCHA iteration is varied between 5,000 and 20,000, depending on the number of FC components. The Helmholtz free energy values obtained from the systematic SSCHA calculations are then fitted to the Rose–Vinet EOS [70]. The temperature range extends from 0 to 1000 K in 50 K intervals. In total, Helmholtz free energy values are computed for 23,583 distinct combinations of structures, volumes, and temperatures. Notably, the polynomial MLP significantly accelerates the energy and force calculations for large sample sets and across a wide range of conditions.

In these SSCHA calculations, we initially employ the optimal MLP used in the global structure search, which exhibits reasonable accuracy for SSCHA calculations. To further improve accuracy, we then develop an MLP specifically optimized for precise predictions of the target structure. This MLP is henceforth referred to as the specialized MLP, while the MLP used in the global structure search is referred to as the general-purpose MLP to distinguish between the two. Due to the high computational cost associated with the DFT calculations required for training, the development of specialized MLPs is limited to 26 structures. These structures are selected based on their Gibbs free energy values, which are within 5 meV/atom of the lowest Gibbs free energy among the set of 81 local minimum structures.

For each structure, we construct a DFT dataset comprising 150–300 randomly generated sample structures using the effective harmonic FCs. Only those FCs that have converged through SSCHA calculations with an MLP and that yield dynamically stable states are utilized. These sample structures are selected to ensure that the specialized MLP adequately covers the entire ranges of volume and temperature. DFT calculations for the sample structures were carried out using the VASP code [63–65] with the same computational settings as those used for constructing the DFT dataset, as detailed in Sec. II C. The cutoff energy was set to 400 eV. The regression coefficients of the polynomial MLP were determined using weighted linear ridge regression, and leave-one-out cross-validation (CV) was utilized to estimate the prediction error, as described in Appendix A. We constructed 285 polynomial MLPs with different single polynomial MLP models. The specialized polynomial MLP with the

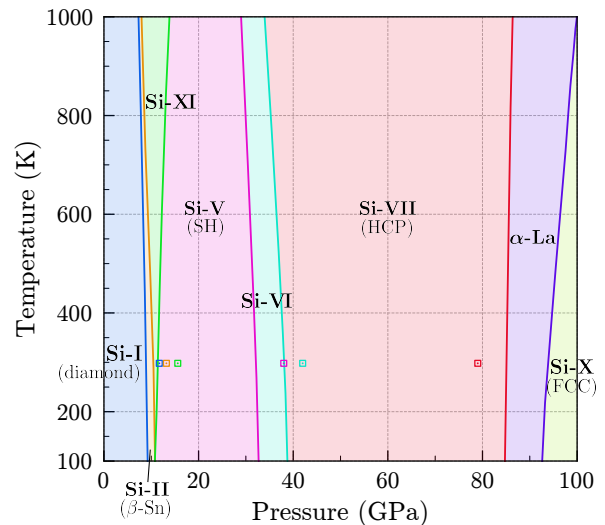


FIG. 12. Pressure-temperature phase diagram calculated using SSCHA calculations with the specialized MLPs for elemental Si. Experimental phase transition pressures [1–3] are shown as open squares, with each square colored to match the corresponding phase boundary for the phase transition observed in the experiments.

lowest CV score was selected for the SSCHA calculations. Using the specialized MLPs, SSCHA calculations were performed over the temperature range from 0 to 1000 K.

C. Phase stability evaluated by the SSCHA

Firstly, we perform SSCHA calculations to compute the Gibbs free energy for 81 local minimum structures with relative enthalpy values less than 30 meV/atom using the general-purpose MLP. Of these 81 local minimum structures, 80 are predicted to be dynamically stable within the SSCHA, which allows us to compute their free energy values. In contrast, only 69 structures are dynamically stable within the harmonic approximation. This result highlights that the SSCHA facilitates free energy calculations for structures stabilized by accounting for the temperature dependence of effective phonon frequencies.

Next, we conduct SSCHA calculations using specialized MLPs to obtain more accurate Gibbs free energy values for 26 local minimum structures. Figure 12 shows the pressure-temperature phase diagram for elemental Si calculated using the SSCHA with the specialized MLPs. The transition pressures at room temperature calculated using the MLPs are similar to the experimental values. At higher temperatures, the pressure ranges where the Si-XI, Si-VII, and α -La-type structures are stable expand. The stable structures identified in the phase diagram correspond to those computed at zero temperature, as listed in Table I.

Figure 13 illustrates the relationship between pressure

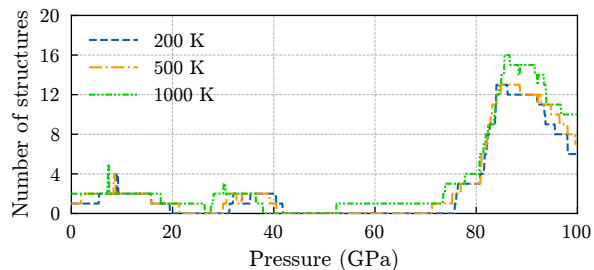


FIG. 13. Relationship between pressure and the number of local minimum structures in elemental Si. Only structures with relative Gibbs free energies below 5 meV/atom are included, excluding the global minimum structure. The pressure ranges from 0 to 100 GPa, and the numbers are shown for temperatures of 200, 500, and 1000 K.

and the number of local minimum structures with relative Gibbs free energies below 5 meV/atom, excluding the global minimum structure. The number of these local minimum structures remains nearly constant as the temperature increases. Additionally, many structures exhibit low relative Gibbs free energies in the 80–100 GPa range, where close-packed structures such as the HCP-, α -La-, and FCC-type structures are stable. The maximum number of local minimum structures with relative Gibbs free energies below 5 meV/atom is 17, observed at 86.5 GPa and 900 K. Among these structures, 16 correspond to those with low relative enthalpy, as shown in Fig. 10, in the pressure range of 80–100 GPa at 0 K.

D. Accuracy of SSCHA calculations

1. Required number of sample structures

In the current SSCHA calculations, the effective FCs are represented by a complete orthonormal basis set $\{\mathbf{b}_1, \mathbf{b}_2, \dots\}$, such that $\boldsymbol{\theta} = \sum_i c_i \mathbf{b}_i$, where c_i denotes the expansion coefficient corresponding to the i -th basis vector. These basis vectors satisfy the permutation symmetry rules, translational sum rules, and the symmetric properties of the supercell [82]. Since a force-displacement dataset from sample structures is used to estimate the expansion coefficients during SSCHA iterations, the number of required sample structures depends on the number of basis vectors, which in turn is determined by both the number of atoms in the supercell and the symmetry properties. When supercells have only a limited number of symmetry operations, the number of basis vectors can become significantly large. Nevertheless, even for such low-symmetry structures, the basis set and the corresponding expansion coefficients can be efficiently obtained using a procedure implemented in the SYMFC code [82].

Figure 14(a) shows the minimum number of force entries in the force-displacement dataset required to achieve FC convergence for the 81 local minimum structures,

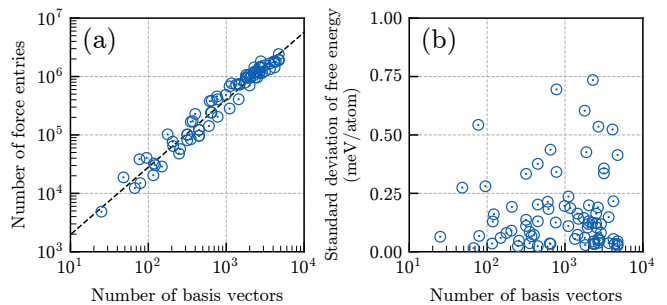


FIG. 14. (a) Minimum number of force entries included in the force-displacement dataset required to achieve convergence of the FCs for the 81 local minimum structures, along with the corresponding number of basis vectors used for FC estimation. The black dotted line represents a linear fit obtained using the least-squares method on logarithmic scales. (b) Standard deviations of the free energy values in SSCHA calculations at 1000 K for the local minimum structures that exhibit dynamically stable states. The standard deviations are derived from free energy values obtained from 10 SSCHA trials, each initiated with random FC values.

along with the corresponding number of basis vectors used for FC estimation. These SSCHA calculations were performed using the general-purpose MLP with a convergence tolerance of 0.01. As depicted in Fig. 14(a), the number of basis vectors ranges from 25 to 4,731 across the 81 structures, and a strong correlation is observed between the number of basis vectors and the number of force entries needed for convergence. In these SSCHA calculations, sample structures containing 64–216 atoms were used. By estimating the required number of sample structures from the number of force entries, it is found that more than half of the local minimum structures require energy and force calculations for at least 1,000 sample structures per iteration to achieve FC convergence at the 0.01 tolerance. If more rigorous convergence tolerances are used, a larger number of sample structures is required. Thus, the use of polynomial MLPs facilitates SSCHA calculations for a wide variety of structures, including low-symmetry structures that require a large number of FC basis vectors.

2. Variance of free energy

Due to the structure sampling approach and the convergence tolerance parameter employed in the SSCHA, the calculated free energy exhibits fluctuations that depend on the specific simulation run. Figure 14(b) presents the standard deviations of the free energy values across the local minimum structures that exhibit dynamically stable states, along with the number of FC basis vectors. The standard deviations are derived from free energy values obtained from 10 independent SSCHA trials started with random FC values. In each trial, the number of sample structures per iteration is set between

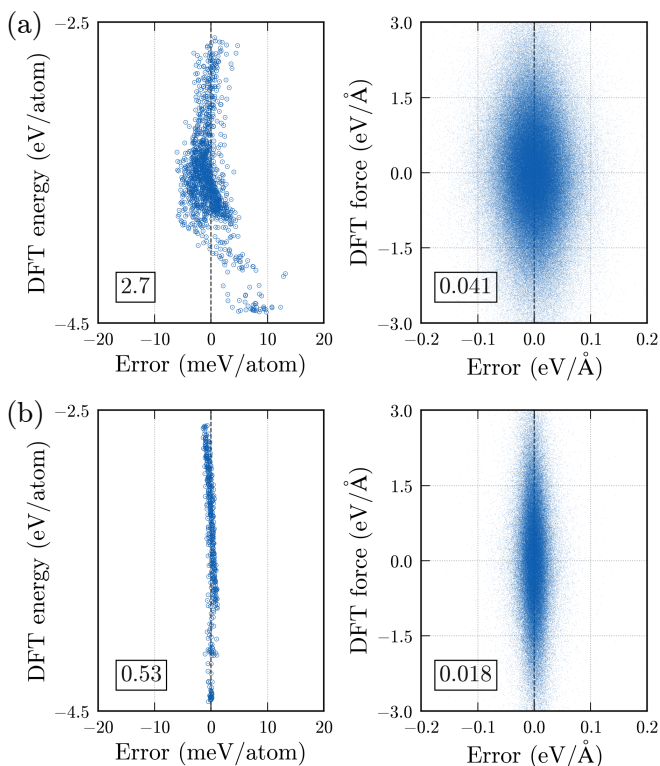


FIG. 15. Error distributions for energy and force values of sample structures in SSCHA calculations for local minimum structures. The energy and force values are computed using (a) the general-purpose MLP and (b) the specialized MLPs, and compared to those obtained from DFT calculations. The numerical values enclosed in the squares indicate RMSEs for energy and force, expressed in meV/atom and eV/Å, respectively.

5,000 and 20,000, as used in the current SSCHA calculations. All standard deviation values are below 1 meV/atom, indicating that the current SSCHA calculations yield robust free energy values. Note that these free energy values are utilized for EOS fittings, and the fitted free energy values are subsequently used to evaluate phase stability. Consequently, errors arising from free energy fluctuations are expected to be minimized through the EOS fitting process.

3. Predictive power

We evaluate the accuracy of both general-purpose and specialized MLPs for SSCHA calculations. In the SSCHA, energy and force values from sample structures are utilized to determine the free energy and effective FCs. Figure 15 illustrates the error distributions for energy and force values from representative sample structures obtained in SSCHA calculations for local minimum structures. For each combination of 81 local minimum structures and 10 to 20 volume conditions, one representative sample structure is selected from those generated by the

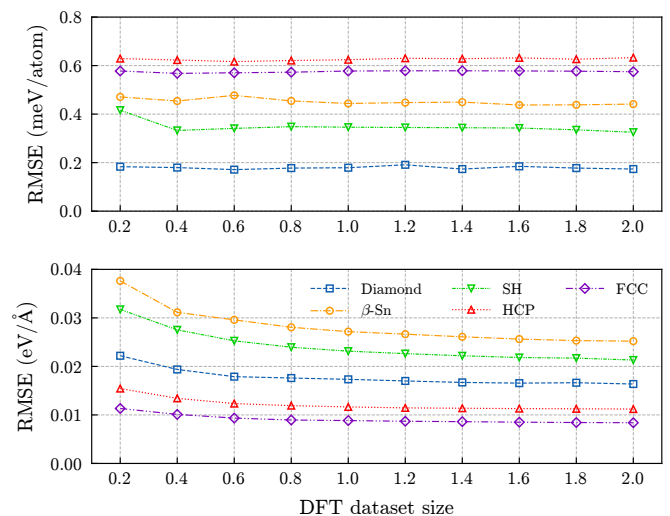


FIG. 16. Relationship between the RMSE evaluated by the cross-validation approach and the DFT dataset size for five local minimum structures. The dataset sizes are expressed as multiples of the current DFT dataset size used in the development of the specialized MLPs. The top and bottom panels show the prediction errors for energy and force, respectively.

converged FCs at 1000 K. In Fig. 15(a), energy and force values computed using the general-purpose MLP are compared with those from DFT calculations. Despite many local minimum structures differing from the prototype structures used to develop the general-purpose MLP, the MLP demonstrates reasonable predictive capability for SSCHA calculations. This indicates that the general-purpose MLP can enable reliable SSCHA calculations across a wide range of local minimum structures. However, prediction errors for energy values tend to be slightly larger for structures with low cohesive energies, which correspond to structures with volumes near equilibrium at low pressure. Figure 15(b) illustrates the performance of the specialized MLPs in predicting the energies and forces of representative sample structures in 26 local minimum structures. As shown in Fig. 15(b), the predictive accuracy of the specialized MLPs is enhanced relative to the general-purpose MLP, thereby enabling more accurate SSCHA calculations.

We also examine the effect of DFT dataset size on prediction errors in constructing the specialized MLPs. Figure 16 shows the relationship between the RMSE evaluated by the cross-validation approach and the DFT dataset size for five local minimum structures. The dataset sizes are expressed as multiples of the current DFT dataset size used to develop the specialized MLPs, ranging from 0.2 to 2.0. The predictive accuracy has sufficiently converged with the current dataset size. Additionally, MLPs developed with dataset sizes as small as 0.4 exhibit reasonable predictive performance, indicating that even smaller datasets can yield sufficiently accurate predictions.

V. CONCLUSION

This study has demonstrated a procedure for performing the efficient and accurate enumeration of crystal structures using polynomial MLPs over a wide range of pressures. Reliable polynomial MLPs, capable of comprehensively enumerating structures across a wide pressure range, have been developed using an iteratively constructed DFT dataset. The dataset includes random structures derived from optimized prototype structures at pressures ranging from 0 to 100 GPa, as well as local minimum structures obtained from RSS. To flexibly represent interatomic interactions in diverse structures, we have proposed hybrid polynomial MLP models that integrate multiple polynomial MLP models. The MLP has successfully identified a variety of globally stable and metastable structures, including almost all experimentally reported structures, with accuracy comparable to DFT calculations.

This study has also introduced a procedure that integrates polynomial MLP to achieve phase stability analysis through global structure search. We have demonstrated the application of this method to evaluate the phase stability of elemental silicon across a temperature range of 0–1000 K and a pressure range of 0–100 GPa, using local minimum structures obtained from the global structure search. In the current approach, the SSCHA method, combined with polynomial MLP, is employed to systematically assess the free energy values of these local minimum structures. The SSCHA method accounts for anharmonic vibrational contributions and enables the evaluation of free energies for dynamically stabilized structures by considering the temperature dependence of effective phonon frequencies. A comprehensive free-energy evaluation of the local minimum structures has yielded a reliable pressure-temperature phase diagram.

The polynomial MLP is crucial to the current approach. This approach involves global structure searches with numerous local geometry optimizations and systematic SSCHA calculations for many structures under various conditions. Additionally, each SSCHA calculation requires the sampling of a large number of supercell structures. Since all these procedures demand extensive energy and force evaluations, the robust polynomial MLPs employed in this study have proven highly efficient in facilitating these processes while maintaining high accuracy. Consequently, this study provides a general and robust framework for reliable crystal structure predic-

tions under pressure and finite-temperature conditions, applicable to a wide range of systems.

ACKNOWLEDGMENTS

This work was supported by a Grant-in-Aid for Scientific Research (A) (Grant Number 21H04621) and a Grant-in-Aid for Scientific Research (B) (Grant Number 22H01756) from the Japan Society for the Promotion of Science (JSPS).

Appendix A: Leave-one-out cross validation

Here, we introduce the weighted leave-one-out CV method to estimate the prediction error of the polynomial MLP. The weighted leave-one-out CV score is defined by

$$(\text{CV score}) = \frac{1}{N_{\text{data}}} \sum_{i=1}^{N_{\text{data}}} \{w_i(\mathbf{x}_i^T \hat{\boldsymbol{\omega}}_{(-i)} - y_i)\}^2, \quad (\text{A1})$$

where N_{data} represents the number of the training data points. \mathbf{x}_i , y_i , and w_i correspond to the predictor vector, the observation value, and the weight for the i -th data point, respectively. The vector $\hat{\boldsymbol{\omega}}_{(-i)}$ denotes the regression coefficients estimated using the dataset excluding the i -th data point.

When calculating the CV score using Eq. (A1), the regression coefficients must be estimated N_{data} times, which can be computationally demanding. However, the CV score for weighted linear ridge regression can be determined by estimating the regression coefficients only once. In this context, the CV score can be rewritten as

$$(\text{CV score}) = \frac{1}{N_{\text{data}}} \sum_{i=1}^{N_{\text{data}}} \left\{ \frac{w_i(\mathbf{x}_i^T \boldsymbol{\omega} - y_i)}{1 - h_{ii}(\lambda)} \right\}^2, \quad (\text{A2})$$

where $h_{ii}(\lambda)$ represents the i -th diagonal element of the hat matrix $H(\lambda)$. The hat matrix is defined as

$$\mathbf{H}(\lambda) = \mathbf{X}(\mathbf{X}^T \mathbf{W}^2 \mathbf{X} + \lambda \mathbf{I})^{-1} \mathbf{X}^T \mathbf{W}^2, \quad (\text{A3})$$

with the symbols explained in Sec. IID. Consequently, the diagonal elements of $H(\lambda)$ can be computed sequentially using

$$h_{ii}(\lambda) = \mathbf{x}_i^T (\mathbf{X}^T \mathbf{W}^2 \mathbf{X} + \lambda \mathbf{I})^{-1} \mathbf{x}_i w_i^2. \quad (\text{A4})$$

-
- [1] M. I. McMahon, R. J. Nelmes, N. G. Wright, and D. R. Allan, Pressure dependence of the Imma phase of silicon, *Phys. Rev. B* **50**, 739 (1994).
 [2] M. Hanfland, U. Schwarz, K. Syassen, and K. Takemura, Crystal Structure of the High-Pressure Phase Silicon VI,

- Phys. Rev. Lett.* **82**, 1197 (1999).
 [3] S. J. Duclos, Y. K. Vohra, and A. L. Ruoff, Experimental study of the crystal stability and equation of state of Si to 248 GPa, *Phys. Rev. B* **41**, 12021 (1990).
 [4] C. J. Pickard and R. J. Needs, High-pressure phases of

- silane, *Phys. Rev. Lett.* **97**, 045504 (2006).
- [5] A. R. Oganov, J. Chen, C. Gatti, Y. Ma, Y. Ma, C. W. Glass, Z. Liu, T. Yu, O. O. Kurakevych, and V. L. Solozhenko, Ionic high-pressure form of elemental boron, *Nature* **457**, 863 (2009).
- [6] W. Zhang, A. R. Oganov, A. F. Goncharov, Q. Zhu, S. E. Boulfelfel, A. O. Lyakhov, E. Stavrou, M. Somayazulu, V. B. Prakapenka, and Z. Konôpková, Unexpected stable stoichiometries of sodium chlorides, *Science* **342**, 1502 (2013).
- [7] J. Lv, Y. Wang, L. Zhu, and Y. Ma, Predicted novel high-pressure phases of lithium, *Phys. Rev. Lett.* **106**, 015503 (2011).
- [8] S. Lorenz, A. Groß, and M. Scheffler, Representing high-dimensional potential-energy surfaces for reactions at surfaces by neural networks, *Chem. Phys. Lett.* **395**, 210 (2004).
- [9] J. Behler and M. Parrinello, Generalized neural-network representation of high-dimensional potential-energy surfaces, *Phys. Rev. Lett.* **98**, 146401 (2007).
- [10] A. P. Bartók, M. C. Payne, R. Kondor, and G. Csányi, Gaussian approximation potentials: The accuracy of quantum mechanics, without the electrons, *Phys. Rev. Lett.* **104**, 136403 (2010).
- [11] J. Behler, Atom-centered symmetry functions for constructing high-dimensional neural network potentials, *J. Chem. Phys.* **134**, 074106 (2011).
- [12] J. Han, L. Zhang, R. Car, and E. Weinan, Deep potential: A general representation of a many-body potential energy surface, *Commun. Comput. Phys.* **23**, 629 (2018).
- [13] N. Artrith and A. Urban, An implementation of artificial neural-network potentials for atomistic materials simulations: Performance for TiO₂, *Comput. Mater. Sci.* **114**, 135 (2016).
- [14] N. Artrith, A. Urban, and G. Ceder, Efficient and accurate machine-learning interpolation of atomic energies in compositions with many species, *Phys. Rev. B* **96**, 014112 (2017).
- [15] W. J. Szlachta, A. P. Bartók, and G. Csányi, Accuracy and transferability of Gaussian approximation potential models for tungsten, *Phys. Rev. B* **90**, 104108 (2014).
- [16] A. P. Bartók, J. Kermode, N. Bernstein, and G. Csányi, Machine Learning a General-Purpose Interatomic Potential for Silicon, *Phys. Rev. X* **8**, 041048 (2018).
- [17] Z. Li, J. R. Kermode, and A. De Vita, Molecular Dynamics with On-the-Fly Machine Learning of Quantum-Mechanical Forces, *Phys. Rev. Lett.* **114**, 096405 (2015).
- [18] A. Glielmo, P. Sollich, and A. De Vita, Accurate interatomic force fields via machine learning with covariant kernels, *Phys. Rev. B* **95**, 214302 (2017).
- [19] A. Seko, A. Takahashi, and I. Tanaka, Sparse representation for a potential energy surface, *Phys. Rev. B* **90**, 024101 (2014).
- [20] A. Seko, A. Takahashi, and I. Tanaka, First-principles interatomic potentials for ten elemental metals via compressed sensing, *Phys. Rev. B* **92**, 054113 (2015).
- [21] A. Takahashi, A. Seko, and I. Tanaka, Conceptual and practical bases for the high accuracy of machine learning interatomic potentials: Application to elemental titanium, *Phys. Rev. Mater.* **1**, 063801 (2017).
- [22] A. P. Thompson, L. P. Swiler, C. R. Trott, S. M. Foiles, and G. J. Tucker, Spectral neighbor analysis method for automated generation of quantum-accurate interatomic potentials, *J. Comput. Phys.* **285**, 316 (2015).
- [23] M. A. Wood and A. P. Thompson, Extending the accuracy of the SNAP interatomic potential form, *J. Chem. Phys.* **148**, 241721 (2018).
- [24] C. Chen, Z. Deng, R. Tran, H. Tang, I.-H. Chu, and S. P. Ong, Accurate force field for molybdenum by machine learning large materials data, *Phys. Rev. Mater.* **1**, 043603 (2017).
- [25] A. V. Shapeev, Moment Tensor Potentials: A Class of Systematically Improvable Interatomic Potentials, *Multiscale Model. Simul.* **14**, 1153 (2016).
- [26] T. Mueller, A. Hernandez, and C. Wang, Machine learning for interatomic potential models, *J. Chem. Phys.* **152**, 050902 (2020).
- [27] A. Khorshidi and A. A. Peterson, Amp: A modular approach to machine learning in atomistic simulations, *Comput. Phys. Commun.* **207**, 310 (2016).
- [28] G. Ferré, J.-B. Maillet, and G. Stoltz, Permutation-invariant distance between atomic configurations, *J. Chem. Phys.* **143**, 104114 (2015).
- [29] S. A. Ghasemi, A. Hofstetter, S. Saha, and S. Goedecker, Interatomic potentials for ionic systems with density functional accuracy based on charge densities obtained by a neural network, *Phys. Rev. B* **92**, 045131 (2015).
- [30] V. Botu and R. Ramprasad, Adaptive machine learning framework to accelerate ab initio molecular dynamics, *Int. J. Quantum Chem.* **115**, 1074 (2015).
- [31] B. Onat, E. D. Cubuk, B. D. Malone, and E. Kaxiras, Implanted neural network potentials: Application to Li-Si alloys, *Phys. Rev. B* **97**, 094106 (2018).
- [32] R. Freitas and Y. Cao, Machine-learning potentials for crystal defects, *MRS Commun.* **10.1557/s43579-022-00221-5** (2022).
- [33] V. L. Deringer, C. J. Pickard, and G. Csányi, Data-Driven Learning of Total and Local Energies in Elemental Boron, *Phys. Rev. Lett.* **120**, 156001 (2018).
- [34] E. V. Podryabinkin, E. V. Tikhonov, A. V. Shapeev, and A. R. Oganov, Accelerating crystal structure prediction by machine-learning interatomic potentials with active learning, *Phys. Rev. B* **99**, 064114 (2019).
- [35] K. Gubaev, E. V. Podryabinkin, G. L. Hart, and A. V. Shapeev, Accelerating high-throughput searches for new alloys with active learning of interatomic potentials, *Comput. Mater. Sci.* **156**, 148 (2019).
- [36] S. Kharabadzé, A. Thorn, E. A. Koulakova, and A. N. Kolmogorov, Prediction of stable Li-Sn compounds: boosting ab initio searches with neural network potentials, *npj Comput. Mater.* **8**, 136 (2022).
- [37] H. Wakai, A. Seko, and I. Tanaka, Efficient global crystal structure prediction using polynomial machine learning potential in the binary Al-Cu alloy system, *J. Ceram. Soc. Jpn.* **131**, 762 (2023).
- [38] A. Seko, Globally stable and metastable crystal structure enumeration using polynomial machine learning potentials for elemental As, Bi, Ga, In, La, P, Sb, Sn, and Te, *Phys. Rev. B* **110**, 224102 (2024).
- [39] A. Seko, Polynomial machine learning potential and its application to global structure search in the ternary Cu-Ag-Au alloy (2024), [arXiv:2407.20630 \[cond-mat.mtrl-sci\]](https://arxiv.org/abs/2407.20630).
- [40] N. R. Werthamer, Self-consistent phonon formulation of anharmonic lattice dynamics, *Phys. Rev. B* **1**, 572 (1970).
- [41] I. Errea, B. Rousseau, and A. Bergara, Anharmonic stabilization of the high-pressure simple cubic phase of calcium, *Phys. Rev. Lett.* **106**, 165501 (2011).

- [42] T. Tadano and S. Tsuneyuki, Self-consistent phonon calculations of lattice dynamical properties in cubic SrTiO_3 with first-principles anharmonic force constants, *Phys. Rev. B* **92**, 054301 (2015).
- [43] D. C. Wallace, *Thermodynamics of crystals* (Dover Publications, 1998).
- [44] P. Choquard, *The anharmonic crystal* (W. A. Benjamin, 1967).
- [45] I. Errea, M. Calandra, and F. Mauri, Anharmonic free energies and phonon dispersions from the stochastic self-consistent harmonic approximation: Application to platinum and palladium hydrides, *Phys. Rev. B* **89**, 064302 (2014).
- [46] R. Bianco, I. Errea, L. Paulatto, M. Calandra, and F. Mauri, Second-order structural phase transitions, free energy curvature, and temperature-dependent anharmonic phonons in the self-consistent harmonic approximation: Theory and stochastic implementation, *Phys. Rev. B* **96**, 014111 (2017).
- [47] L. Monacelli, R. Bianco, M. Cherubini, M. Calandra, I. Errea, and F. Mauri, The stochastic self-consistent harmonic approximation: calculating vibrational properties of materials with full quantum and anharmonic effects, *J. Phys.: Condens. Matter* **33**, 363001 (2021).
- [48] A. Seko, A. Togo, and I. Tanaka, Group-theoretical high-order rotational invariants for structural representations: Application to linearized machine learning interatomic potential, *Phys. Rev. B* **99**, 214108 (2019).
- [49] A. Seko, Machine learning potentials for multicomponent systems: The Ti-Al binary system, *Phys. Rev. B* **102**, 174104 (2020).
- [50] T. Nishiyama, A. Seko, and I. Tanaka, Application of machine learning potentials to predict grain boundary properties in fcc elemental metals, *Phys. Rev. Mater.* **4**, 123607 (2020).
- [51] S. Fujii and A. Seko, Structure and lattice thermal conductivity of grain boundaries in silicon by using machine learning potential and molecular dynamics, *Comput. Mater. Sci.* **204**, 111137 (2022).
- [52] H. Wakai, A. Seko, H. Izuta, T. Nishiyama, and I. Tanaka, Predictive power of polynomial machine learning potentials for liquid states in 22 elemental systems, *Phys. Rev. B* **109**, 214207 (2024).
- [53] A. Seko, Tutorial: Systematic development of polynomial machine learning potentials for elemental and alloy systems, *J. Appl. Phys.* **133**, 011101 (2023).
- [54] M. El-Batanouny and F. Wooten, *Symmetry and Condensed Matter Physics: A Computational Approach* (Cambridge University Press, Cambridge, 2008).
- [55] G. P. P. Pun, R. Batra, R. Ramprasad, and Y. Mishin, Physically informed artificial neural networks for atomistic modeling of materials, *Nat. Commun.* **10**, 2339 (2019).
- [56] M. S. Nitol, K. Dang, S. J. Fensin, M. I. Baskes, D. E. Dickel, and C. D. Barrett, Hybrid interatomic potential for Sn, *Phys. Rev. Mater.* **7**, 043601 (2023).
- [57] B. Narayanan, A. Kinaci, F. G. Sen, M. J. Davis, S. K. Gray, M. K. Y. Chan, and S. K. R. S. Sankaranarayanan, Describing the Diverse Geometries of Gold from Nanoclusters to Bulk—A First-Principles-Based Hybrid Bond-Order Potential, *J. Phys. Chem. C* **120**, 13787 (2016).
- [58] M. Wen and E. B. Tadmor, Hybrid neural network potential for multilayer graphene, *Phys. Rev. B* **100**, 195419 (2019).
- [59] D. Zagorac, H. Müller, S. Ruehl, J. Zagorac, and S. Rehme, Recent developments in the Inorganic Crystal Structure Database: theoretical crystal structure data and related features, *J. Appl. Crystallogr.* **52**, 918 (2019).
- [60] P. E. Blöchl, Projector augmented-wave method, *Phys. Rev. B* **50**, 17953 (1994).
- [61] G. Kresse and D. Joubert, From ultrasoft pseudopotentials to the projector augmented-wave method, *Phys. Rev. B* **59**, 1758 (1999).
- [62] J. P. Perdew, K. Burke, and M. Ernzerhof, Generalized Gradient Approximation Made Simple, *Phys. Rev. Lett.* **77**, 3865 (1996).
- [63] G. Kresse and J. Hafner, Ab initio molecular dynamics for liquid metals, *Phys. Rev. B* **47**, 558 (1993).
- [64] G. Kresse and J. Furthmüller, Efficient iterative schemes for ab initio total-energy calculations using a plane-wave basis set, *Phys. Rev. B* **54**, 11169 (1996).
- [65] G. Kresse and J. Furthmüller, Efficiency of ab-initio total energy calculations for metals and semiconductors using a plane-wave basis set, *Comput. Mater. Sci.* **6**, 15 (1996).
- [66] A. Seko, <https://github.com/sekocho/pypolymlp>.
- [67] A. Togo and I. Tanaka, First principles phonon calculations in materials science, *Scr. Mater.* **108**, 1 (2015).
- [68] F. Glover and G. A. Kochenberger, *Handbook of Metaheuristics* (Springer New York, 2003).
- [69] E. Fjaer, R. M. Holt, P. Horsrud, and A. M. Raaen, *Petroleum related rock mechanics* (Elsevier, 2008).
- [70] P. Vinet, J. R. Smith, J. Ferrante, and J. H. Rose, Temperature effects on the universal equation of state of solids, *Phys. Rev. B* **35**, 1945 (1987).
- [71] D. Töbrens, N. Stüßer, K. Knorr, H. Mayer, and G. Lampert, E9: The New High-Resolution Neutron Powder Diffractometer at the Berlin Neutron Scattering Center, in *European Powder Diffraction EPDIC 7*, Mater. Sci. Forum, Vol. 378 (Trans Tech Publications Ltd, 2001) pp. 288–293.
- [72] J. C. Jamieson, Crystal Structures at High Pressures of Metallic Modifications of Silicon and Germanium, *Science* **139**, 762 (1963).
- [73] H. Olijnyk, S. Sikka, and W. Holzappel, Structural phase transitions in Si and Ge under pressures up to 50 GPa, *Phys. Lett. A* **103**, 137 (1984).
- [74] S. J. Duclos, Y. K. Vohra, and A. L. Ruoff, hcp to fcc transition in silicon at 78 GPa and studies to 100 GPa, *Phys. Rev. Lett.* **58**, 775 (1987).
- [75] M. I. McMahon and R. J. Nelmes, New high-pressure phase of Si, *Phys. Rev. B* **47**, 8337 (1993).
- [76] A. Wosylus, H. Rosner, W. Schnelle, and U. Schwarz, Crystal Structure Refinement and Electronic Properties of Si(cI16), *Z. Anorg. Allg. Chem.* **635**, 700 (2009).
- [77] J. Crain, G. J. Ackland, J. R. Maclean, R. O. Piltz, P. D. Hatton, and G. S. Pawley, Reversible pressure-induced structural transitions between metastable phases of silicon, *Phys. Rev. B* **50**, 13043 (1994).
- [78] M. Guerette, M. D. Ward, L. Zhu, and T. A. Strobel, Single-crystal synthesis and properties of the open-framework allotrope Si₂₄, *J. Phys.: Condens. Matter* **32**, 194001 (2020).
- [79] H. M. Jennings and M. H. Richman, A Hexagonal (Wurtzite) Form of Silicon, *Science* **193**, 1242 (1976).
- [80] E. Y. Tonkov and E. Ponyatovsky, *Phase Transformations of Elements under High Pressure* (CRC press, 2018).

- [81] A. van Roekeghem, J. Carrete, and N. Mingo, Quantum self-consistent ab-initio lattice dynamics, *Comput. Phys. Commun.* **263**, 107945 (2021).
- [82] A. Seko and A. Togo, Projector-based efficient estimation of force constants, *Phys. Rev. B* **110**, 214302 (2024).